Proceedings of 2022 Hypervelocity Impact Symposium
HVIS2022
September 18-22, 2022, Alexandria, VA, USA

HVIS2022-10

THE EFFECTS OF PROJECTILE LEADING EDGE AND ASPECT RATIO ON THE DEFLECTION EFFICIENCY OF PLANETARY SCALE HYPERVELOCITY IMPACTS

Mallory E. DeCoster[1], Tony Le[1], Dawn Graninger[1], Patrick King[1], Angela Stickle[1]

[1]Johns Hopkins University Applied Physics Lab, Laurel, MD USA

ABSTRACT

The influence of mission design parameters on the deflection efficiency of hypervelocity kinetic impacts remains an open question. With the upcoming impact of NASA's Double Asteroid Redirection Test (DART), great interest exists in understanding how to optimize the deflection of a potentially hazardous object. In this work, we investigate the influence of projectile geometry on three-deflection efficiency observable using 2D simulations with the CTH hydrocode. We vary both the angle between the target and leading edge of the projectile in addition to the aspect ratio, to understand the projectile geometry effects on a kinetic impact. We show evidence for a projectile geometry effect on deflection efficiency observables that is highly dependent on the target material composition, where an enhancement of 5% in β is achieved in strong targets (cohesion=10 MPa), and 28% in weak targets (cohesion=100 Pa). The deflection efficiency is positively correlated to α ***and the projectile aspect ratio****, where the sphere and tall rod emerged as the most efficient projectiles in strong and weak targets.*

Keywords: Kinetic impactor, hypervelocity **impact**, planetary defense, projectile geometry

NOMENCLATURE

α	angle between the target and projectile surface
AR	aspect ratio **(length/diameter)**
β	momentum enhancement factor (β)
m	ejecta mass
M	projectile mass
m_T	target mass
P_T	target momentum
v	ejecta velocity
U	impact velocity
v_T	target velocity
Y_o	cohesive strength
σ	tensile strength

1. INTRODUCTION

The upcoming impact of NASA's Double Asteroid Redirection Test (DART) spacecraft with its intended target, paired with internationally spurred interest in planetary defense have drawn attention to the reality that asteroid impacts are a potentially preventable serious natural hazard.[1] The kinetic impact method for deflecting a potentially hazardous object (PHO) involves sending a high-speed spacecraft into the path of the approaching PHO to deflect it onto a different, non-threatening, trajectory. Overall, the kinetic impact method is a promising strategy for asteroid deflection that exhibits a high degree of technological maturity.[2,3] Currently, there are few experimental and computational investigations reported on the role of mission design parameters coupled with variations in target material properties, on the deflection efficiency of a kinetic impactor. [4–6] The successful impact of the DART spacecraft, on September 26, 2022, with Dimorphos (the secondary moonlet of the binary Didymos asteroid system) will be the first full scale experimental test of the kinetic impactor technology in understanding its viability towards asteroid deflection. However, additional computational studies are required to inform current and future missions planned by the planetary defense community.

The relative velocity vector of the projectile and the momentum enhancement factor (β) are most responsible for determining the deflection efficiency (i.e., velocity change of the orbit of the PHO) resulting from a kinetic impact. Momentum enhancement occurs when a projectile strikes a target at hypervelocity.[7] β is a non-dimensional value that measures the amount of additional momentum transferred to the target by thrust generated from ejecta moving in the opposing direction to the target. Equation 1 shows the analytical definition of β is a function of the instantaneous change in velocity of the target (Δv_T), the target mass (m_T), and the projectile momentum (MU), which can also be represented by the ejecta mass (m) and velocity (v).[8,9]

HVIS2022-10

$$\beta = \frac{\Delta P_T}{MU} = \frac{m_T \Delta v_T}{\mathrm{M}U} = 1 + \frac{\mathrm{m}v}{MU} \quad (1)$$

Since β contains components from both the projectile and ejecta momentum, β = 1 indicates that only the projectile momentum was transferred while β > 1 implies additional momentum was transferred due to ejecta. Previous studies have shown that β is highly dependent on target properties, such as the local topography at the impact site and material parameters like cohesive strength, internal friction, and porosity, which a kinetic impactor mission has little design control over.[6,8,10,11] However, the extent to which β can be optimized by mission design parameters that can be controlled for (i.e. spacecraft geometry) remains an open question. To this end, we investigated the role of both aspect ratio (AR=**length/diameter**) and the contact angle between the leading edge of the projectile with the target surface (α) on three deflection efficiency observables: β, ejecta mass-velocity distribution, and cratering efficiency. ***α* is the angle formed between the surface tangent of the target to the leading edge of the projectile (Figure 1)**. **Depending on the complexity of the projectile shape, *α* can be static (cone, flat plate, tall rod) or dynamic (sphere).**

This manuscript reports results from a 2D computational study that used CTH to investigate the effect of varying α and the aspect ratio of the projectile on three deflection efficiency observables. We varied the target strength by five orders of magnitude to test the effects of projectile geometry as a function of the target morphological parameters, which have been shown to play a major role in determining the resulting deflection efficiency observables.[10,13] We show that there is evidence for a projectile geometry effect that is highly dependent on target strength. The effects of projectile geometry are dampened in the strong target, however in the weak target, we find that β is positively correlated with **both** α and **the projectile** aspect ratio. Interestingly, we also find that cratering efficiency does not necessarily predict deflection efficiency, where excavated material can remain attached to the crater lip and not contribute to ejecta. These results uncover both limitations and opportunities **for how to optimize the deflection efficiency of a kinetic impact by adjusting mission design parameters.** Understanding how to tune relevant parameters is crucial for the next generation kinetic impactors to fulfil their promise as the most practical and mature technology (excluding for civil defense actions) for threat mitigation.

2. MATERIALS AND METHODS

This section describes the details of the modeling and simulations tools and analysis techniques used to investigate the role of projectile geometry on the deflection efficiency of a kinetic impactor at planetary defense scales.

2.1 Numerical Model

We used CTH to perform two-dimensional axisymmetric simulations of planetary defense scale kinetic impacts into asteroid like surfaces. In brief, CTH is an Eulerian, large deformation, strong shock wave physics code developed by Sandia National Laboratories and commonly used to simulate hypervelocity impacts.[9,14–16] The development history and description of the models and novel features of CTH are described in detail elsewhere.[12,15] The simulations did not include gravity and occurred in the strength-dominated regime. **Previous case studies show general convergence between hypervelocity impacts modeled by 2D axisymmetric and 3D grids in CTH.[12] However, it is important to note that symmetry can be quickly lost in brittle target materials due to changing facture behavior, or for non-normal impacts, which require computationally more expensive 3D grids.**

We used CTH's adaptive mesh refinement (AMR) capability to define areas of high and low-resolution within the mesh that result in the ability to resolve select areas (i.e. shock wave and material interfaces) for improved accuracy while also balancing computational resources. Therefore, the spatial resolution in our AMR grids was dynamic. The highest spatial resolution was set based on how many cells per projectile radius (cppr) were used to represent the projectile shape. Since the radius of the projectile was typically much larger than the length scale associated with its leading edge, we choose a cppr=10 for the cylinders and sphere and a cppr=20 for the cone for impacts into strong targets, and a cppr=30 for all impacts into weak target. This balanced computational efficiency with numerical precision.[9] Table 1 details eight test cases defined by a traditional parameter sweep that varied the angle α and the aspect ratio (AR), simulated using the CTH shock physics code. While the projectile volume changes as a function of geometry, the projectile mass, material type, and impact velocity were held constant to 500 kg, Aluminum, and 6.65 km/s respectively.

Table 1: CTH TEST MATRIX. THE PROJECTILE MASS AND IMPACT VELOCITY WERE HELD CONSTANT AT 500 KG, AND 6.65 KM/S RESPECTIVELY, THE STRONG TARGET HAD Y_O=10 MPA AND THE WEAK TARGET HAD Y_O= 100 PA.

Projectile Shape	α (^{O})	AR (L/D)	Length (cm)	Diameter (cm)	Target Strength
Flat plate	0	0.25	24.5	98.1	Strong
Flat plate	0	0.25	24.5	98.1	Weak
Tall rod	90	2.50	113.8	45.5	Strong
Tall rod	90	2.50	113.8	45.5	Weak
Cone	45	0.50	56.3	112.7	Strong
Cone	45	0.50	56.3	112.7	Weak
Sphere	0-90	1	-	70.62	Strong
Sphere	0-90	1	-	70.62	Weak

HVIS2022-10

2.2 Projectile Geometry

Previous studies have shown that the resulting impact flash (intense short duration flash of visible radiation at impact) from a hypervelocity impact is related to the geometry of the colliding surface of the projectile and target.[17] Although the phenomena responsible for impact flashes are fundamentally different from cratering mechanisms,[18] we take this as evidence to formulate a hypothesis that the angle between the target and leading edge of the projectile may result in a projectile geometry effect to the deflection efficiency observables resulting from a hypervelocity kinetic impact. Therefore, we explored this effect by modeling a set of simple projectile shapes (cylinders (flat plate/tall rod), cone, and sphere) that formed varying angles between their leading edge and the target surface (α). Figure 1 shows a schematic of the 2D axisymmetric projectile shapes investigated, and their corresponding α values. Note that the sphere had a dynamic α ranging from 0° at the moment of impact, to 90° when the projectile had penetrated half its diameter distance into the target surface. Additionally, we also varied the aspect ratio (AR) of the cylinders in order to create two endmembers representing a flat plate (AR=**0.25**, α=0°) and a tall rod (AR=**2.50**, α=90°).

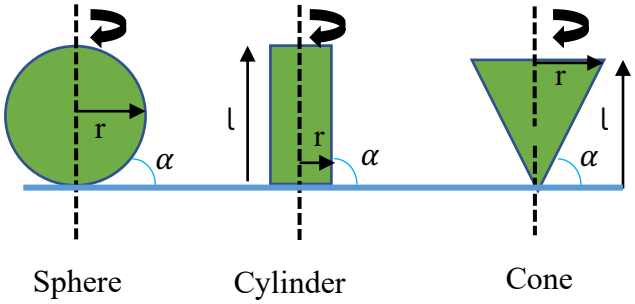

Figure 1: SCHEMATIC OF THE 2D AXISYMMETRIC PROJECTILE STRUCTURES INVESTIGATED IN THIS WORK. THE RADIUS 'R' (**DIAMETER =2R**) AND **LENGTH 'l'** ARE LISTED FOR EACH SHAPE AS WELL AS THE ANGLE BETWEEN THE PROJECTILE LEADING EDGE AND TARGET SURFACE (α).

The projectiles investigated consisted of 500 kg of non-porous aluminum impacting a spherical basalt target at 6.65 km/s. The projectiles were represented by the SESAME equation of state (EOS) for Aluminum,[19,20] which is widely used in impact simulations.[21] The SESAME EOS is a tabular database constructed from the three-component Helmholtz free energy EOS model that relates pressure and internal energy to temperature. Additionally, we used the Steinberg-Guinan-Lund (SGL) strain-rate constitutive model for '1100-0 Aluminum', which was defined as a standard option within CTH.[22–24]. The full details of the projectiles are summarized in **Tables 1- 2**.

2.3 Target Material Model

Previous studies have shown that target morphology (i.e. cohesive strength, porosity, internal friction) plays a much greater role in determining deflection efficiency phenomena from a hypervelocity impact compared to composition.[6,10] Therefore, while the range of the composition of realistic asteroids includes carbonaceous (B-type), silicaceous (S-type),

Table 2: MATERIAL MODEL PARAMETERS USED FOR CTH SIMULATIONS

Description	***Impactor***	***Target***
Material	Al	Basalt
Equation of state	SESAME	SESAME
Mass (kg)	500	$1.88e^{6}$
Impact velocity (km/s)	6.65	-
Strength model	SGL	BDL/none
Density ($\frac{g}{cm^3}$)	2.700	2.124
Porosity (%)[a]	0	30
Poisson ratio	0.33	0.25
SGL Strength Parameters		
Internal yield stress, $Y_0(MPa)$	260	-
Max. Yield stress, $Y_M(MPa)$	760	-
Internal shear modulus, $G_0(GPa)$	28.6	-
Material constant, A $((Pa)^{-1})$	$6.52e^{-13}$	-
Material constant, B $((eV)^{-1})$	7.15	-
Initial Gruneisen coefficient	2.00	-
Melting temperature at constant volume, T_m (eV)	0.1051	-

Target Strength Parameters	**BDL**	**EPPVM**
Shear strength at zero pressure, $Y_{i0}(MPa)$	-	10	$1e^{-4}$
von Mises plastic limit, $Y_m(GPa)$	-	3.5	-
Coefficient of internal friction of intact rock	-	1.8	-
Coefficient of internal friction (damaged), μ_d	-	0.8	-
Tensile strength, (MPa)	-	-10	$-1e^{-4}$
Strength at infinite pressure, $Y_{inf}(GPa)$	-	2.5	-
Damage at failure	-	0.7	-
Melting temperature, (eV)		0.16	0.16

[a] The P-α model was used to represent the porosity[27]

and nickel-iron (M-type), the morphological construct is far more important. Results from recently visited asteroids like Bennu (B-type) and Ryugu (B/C-type) exhibited very weak cohesive strengths, on the order of a few to a few hundred Pa.[25,26] Additionally, Earth and space based observations along with asteroid sample returns have revealed that asteroids vary tremendously in porosity, ranging from non-porous monolithic solid rocks to highly porous rubble piles (65-85%).[28–31] Porosity attenuates shock propagation, which can greatly affect the cratering process.[30] Therefore, in order to represent realistic asteroid-like material, we defined two 160 m diameter spheres of porous basalt (S-type) with strong (Y_o=10 MPa) and weak (Y_o=100 Pa) cohesive strength (see Table 2). Note the tensile strength was also adjusted to be within the same order of magnitude of the cohesive strength, which is typical of geologic material and has been shown to play an important role in kinetic impact studies.[32,33] In CTH, the targets were modeled as 30% porous basalt represented by the SESAME EOS.[20] The stronger basalt target used the Brittle Damage with Localized Thermal Softening (BDL) constitutive model,[34,35] which includes a pressure-dependent yield and brittle damage model based on the strength/damage model described by Collins et al.[36] The weaker target used the Basalt Sesame EOS and the elastic-perfectly plastic with von Mises yield surface model (EPPVM) to define the limiting yield strength, and no damage model.

2.4 Ejecta and Crater Measurements

The deflection efficiency observables calculated and reported in this work include the momentum enhancement factor (β), the distribution of ejecta mass and velocity, and the cratering efficiency. The analysis performed in this work follows the protocol described in DeCoster et al. 2022.[4] In brief, ejecta material were defined as any material containing a void fraction greater than zero but less than one, with positive upward velocity (positive y-direction) that existed above a predefined ejecta plane. The ejecta plane was set to y=80 cm for the strong and y=200 cm for the weak targets in order to avoid classifying material that was uplifted but stayed attached to the crater lip, as ejecta. Additionally, ejecta that left the spatial domain of the mesh was accounted for by virtual witness plates placed at the mesh boundary, which tracked the mass and velocity of each ejecta particle as it left the grid. β was calculated according to Equation 1, where the ejecta mass (m) and velocity (v) consisted of ejecta material that both remained in and had left the grid.

The temporal evolution of the transient crater for each simulation was calculated from an algorithm that measured the depth and the width of the crater by tracking the cells forming the boundary between the target material and void. The depth represented the distance from the impact plane (y = 0) to the maximum absolute value of the height location for the boundary cells, and the diameter represented the distance between cells along the crater boundary profile that intersected the impact plane.

3 RESULTS AND DISCUSSION

This section details the results from eight CTH hydrocode simulations that investigated the projectile geometry effects of α and aspect ratio on deflection efficiency.

3.1 Momentum Enhancement Factor (β)

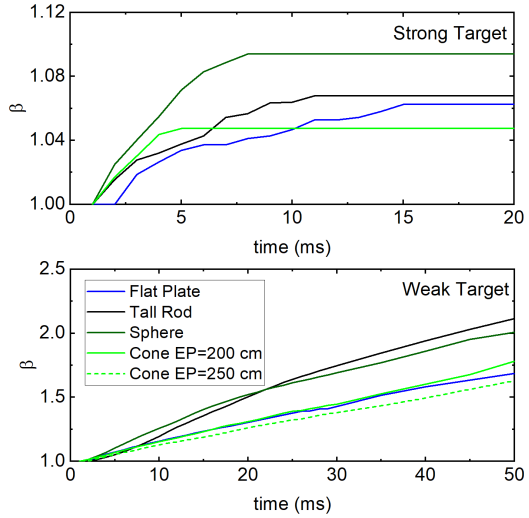

Figure 2: TEMPORAL EVOLUTION OF β INTO STRONG (TOP) AND WEAK (BOTTOM) TARGETS.

β is a non-dimensional term that provides information about the efficiency of a kinetic impact. Figure 2 plots the temporal evolution of β for four projectile geometries into strong and weak targets. As expected, projectiles impacting weaker targets resulted in larger β's because the weaker cohesion and tensile strength made it possible to fracture and eject more target material that transfered momentum to the target.[6] Both the sphere and tall rod were the most efficient projectile geometries and the cone and flat plate were the least efficient when impacting strong and weak targets. The spherical projectile was the most efficient projectile geometry in the strong target, where it was ~5% more effective compared to the worst performing projectile (cone). The tall rod and sphere were 26% and 18% more efficient respectively, compared to the flat plate impacting the weak target. The cone was one of the least efficient projectile geometries for both targets. Inspection of the craters formed by the cone into a weak target (Figure 5) indicated that a large crater lip formed following the impact that extended vertically beyond 200 cm (where the ejecta plane is set). Material that was attached to the crater lip was not considered ejecta material and did not

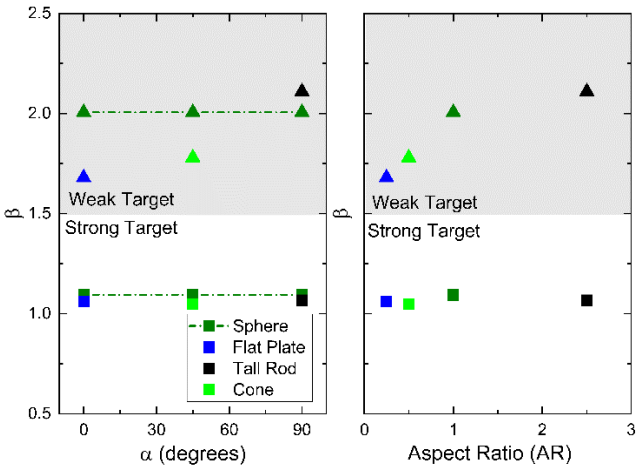

Figure 3: β VS. α (LEFT) AND ASPECT RATIO (RIGHT) FOR ALL FOUR PROJECTILE GEOMETRIES.

contribute to β. Therefore, Figure 2 shows the temporal evolution of β with the ejecta plane set to 250 cm, to showcase the effects of properly differentiating between ejecta material and the crater lip. We note however, that the material making up the extended crater lip may detach at later times, and may drastically improve the β achieved for the cone. Further studies are required to investigate the effects of projectile shape on the form of the crater rim. Additionally, our results are in line with previous computational work from Walker and Chocron, that found that spherical aluminum projectiles impacting water ice targets (Y_o=2 MPa) at 10 km/s resulted in ~75% higher β values compared to projectiles consisting of flat plates (AR=0.25).[33] Our results provide evidence for a projectile geometry effect on β, which is more pronounced in weak targets than in strong targets.

Figure 3 plots β as a function of α and as a function of aspect ratio (AR) for projectiles impacting strong and weak targets. The effects of α and AR on β are negligible (<5%) for projectiles impacting strong targets. In the weak target regime however, β increases with α and the projectile aspect ratio. Together, the tall rod (large α and **large** AR) and sphere (dynamic α, **large** AR), led to the largest β's suggesting that projectile shapes such as ogives, with curved leading edges and **large** AR may present an avenue for optimizing β. Further investigation is **underway** to differentiate between the response of β to projectile AR and α, to determine which parameter is the most significant.

3.2 Ejecta Mass and Velocity Distribution

In order to understand the influence of projectile geometry on β, we plot the cumulative ejecta mass vs. ejecta velocity in the direction normal to the target surface at impact, where the ejecta mass (m) is normalized by the projectile mass

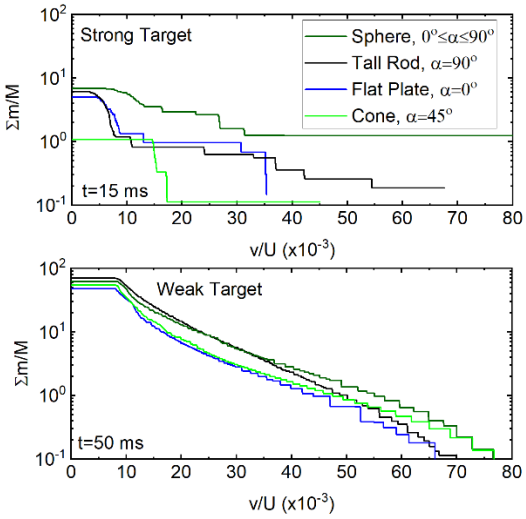

Figure 4: CUMULATIVE EJECTA MASS (m) NORMALIZED BY THE PROJECTILE MASS (M) VS. EJECTA VELOCITY (v) NORMALIZED BY THE IMPACT VELOCITY (U), PLOTTED AT 15 MS FOR THE STRONG TARGETS, AND 50 MS FOR THE WEAK TARGETS.

(M), and the ejecta velocity (v) is normalized by the impact velocity (U). Since the evolution of the transient crater occured at different time scales in each targets, the ejecta mass and velocity distribution are plotted at different time intervals that are informed by the temporal evolution of the transient crater (Figure 6). Figure 4 shows that the amount of ejecta mass was related to β, where projectiles that produced the most ejecta mass also exhibited the highest β's in both strong and weak targets. In general, projectiles impacting the weak target excavated about an order of magnitude more ejecta material compared to the strong target, however this only resulted in roughly a factor of 2 increase in β. Within the strong target regime, the two most efficient projectile geometries resulted in very different ejecta mass-velocity distributions (i.e. their large β values seem to be due to different reasons). While both projectile geometries excavated roughly the same amount of ejecta mass, the sphere imparted a much larger velocity component to its ejecta overall (i.e. more ejecta material that is moving faster), compared to the tall rod, which had a large population of slower moving ejecta ($v/U \leq 10\text{x}10^{-3}$). The cone resulted in the least amount of ejecta material, where most of the excavated material remained attached to the crater lip (see section 3.3). A similar phenomenon occurred in the weak target, where the sphere resulted in a very fast population of ejecta ($v/U > 40\text{x}10^{-3}$) compared to the tall rod. Here however, the tall rod emerged as more efficient (higher β) due to a larger population of slower moving ejecta (v/U= 10-21x10^{-3}). The flat plate and cone resulted in both the least total ejecta mass, and also produced an ejecta cloud with relatively smaller velocities compared to the sphere and tall rod.

HVIS2022-10

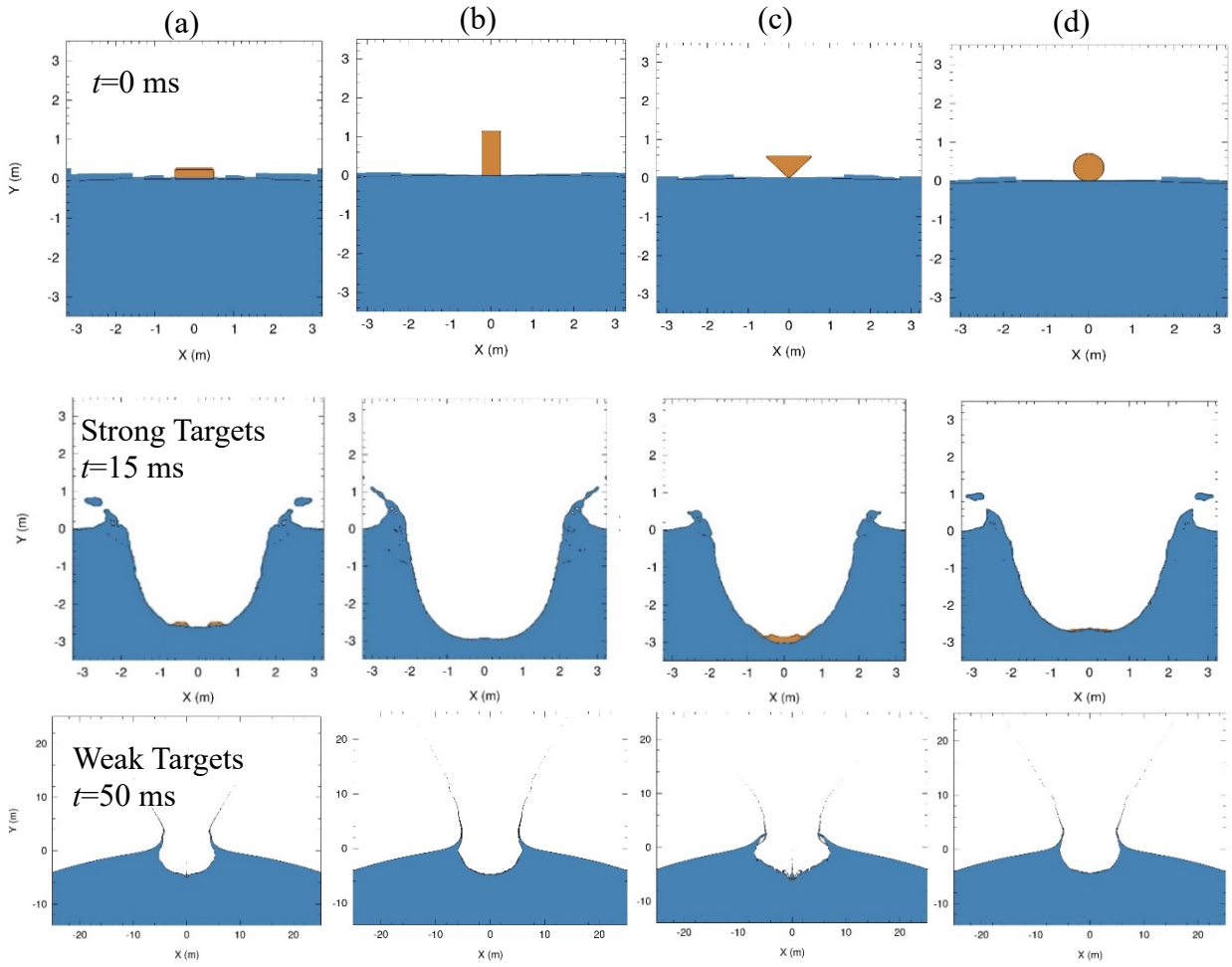

FIGURE 5: TRANSIENT CRATERS (TOP ROW) PRE IMPACT, (MIDDLE ROW) 15 MS POST IMPACT INTO STRONG TARGETS, AND (BOTTOM ROW) 50 MS POST IMPACT INTO WEAK TARGETS FOR (A) FLAT PLATE, (B) TALL ROD, (C) SPHERE, AND (D) CONE PROJECTILES. THE ALUMINUM PROJECTILES ARE SHOWN IN ORANGE, AND THE BASALT TARGET MATERIAL IS SHOWN IN BLUE.

We do note that the cone appeared to gain efficiency when impacting a weak target vs. the strong, where it produced an ejecta mass-velocity profile that was more similar to the other projectile geometry profiles. In the strong target regime, the ejecta mass-velocity distribution produced by the cone was quite stunted compared to other projectile geometries.

Figure 4 shows that the **larger projectile** aspect ratio results in the excavation of more ejecta mass, however the effects on the ejecta velocity varied as a function of both α and target strength. Generally, weaker targets resulted in larger populations of faster moving ejecta that contributed to increasing β. In both targets, the spherical projectile imparted the largest velocities to its ejecta, which suggests a dynamic α may be desirable. The cone (α=45°) was one of the most inefficient projectile in both targets, producing a relatively small amount of ejecta exhibiting slow velocities, however it became much more efficient in the weak target, where it excavated more ejecta than the flat plate.

3.3 Cratering Efficiency

We investigated the influence of projectile geometry on cratering efficiency to provide insight to the results presented in sections 3.1-3.2. The transient crater is significant because its

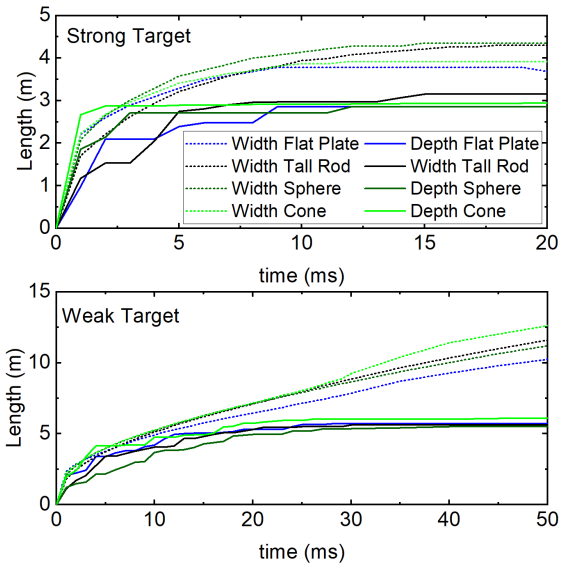

Figure 6: TEMPORAL EVOLUTION OF THE CRATER PROFILE (WIDTH AND DEPTH) FOR PROJECTILES IMPACTING STRONG (TOP) AND WEAK (BOTTOM) TARGETS.

size is considered to be the measure of the crater that best reflects the kinetic energy/momentum of the projectile.[37] Figure 5 illustrates the transient craters formed in strong and weak targets at 15 ms and 50 ms post impact respectively. Both targets resulted in bowl shaped transient craters. For the strong targets, Figure 5 clearly shows that the tall rod resulted in the deepest crater, however all four projectiles produced very similar crater profiles. In the weak target, Figure 5 shows that the cylinders and sphere resulted in similar crater profiles, however the cone was an outlier, where the crater lip extended out horizontally over the crater void. This difference in the behavior of the crater lip may explain why the cone was the worst performer, where the spatial extent of the crater lip might deflect additional ejecta material from rising above the ejecta plane.

Figure 6 provides a quantitative representation of the cratering efficiency to help clarify the role of projectile geometry on cratering. First, monitoring the temporal evolution for the asymptote of width and depth of the transient crater allows for the determination of the time interval where the transient crater is done forming and the simulation can be stopped.[37] Figure 6 shows that the transient craters were finished evolving by ~15 ms for the strong targets, and approximately 50 ms in the weak targets (when the crater depth had reached a maximum, however we note the width may still be evolving). Interestingly, for both strong and weak targets respectively, all projectiles resulted in approximately the same depth profiles, but varying crater widths.

Consistent with previous trends in β and ejecta mass, the projectiles that resulted in the highest β values and largest ejecta mass (sphere and tall rod) also exhibited the highest cratering efficiency (i.e. largest volume) in both target material, with one exception- the cone. Although the cone emerged as the least efficient projectile, it surprisingly exhibited the highest cratering efficiency. Further inspection indicated that the large amount of material excavated to form the crater ended up forming and staying attached to the crater lip, and did not contribute to the ejecta. This interesting result suggests that the cone could potentially become a highly effective projectile if the large amount of excavated material forming the crater lip were to detach and become ejecta. Indeed, we see that the crater width was still evolving, and running out these models to a longer time scale may yield increased β values for the cone. Further, the tall rod and sphere resulted in higher crater efficiency compared to the cone (in the strong target) and flat plate (in both targets). In general, the largest craters (highest cratering efficiencies) corresponded to the projectiles that generated the most ejecta mass in the strong target, however large craters didn't always correspond to large ejecta masses in weak targets, where excavated material may remain attached to the crater lip so that it does not contribute to the ejecta distribution and β.

4. CONCLUSION

We investigated the effects of projectile geometry on three deflection efficiency observables (β, ejecta mass-velocity distribution, and crater efficiency) resulting from planetary defense scale hypervelocity impact using hydrocode simulations performed in CTH. Specifically, we varied the angle between the leading edge of the projectile and target (α), and the aspect ratio. We find evidence for a projectile geometry effect that is most pronounced in weak targets. According to the projectile geometries studied here, β increase with both α and **the** projectile aspect ratio. While the role of α on ejecta mass-velocity distributions is complex, **larger** aspect ratios lead to larger amounts of ejecta mass, with the sphere and tall rod excavated the most material in both strong and weak targets. Notably, the cone projectile geometry resulted in a smaller β (and ejecta mass) but had the highest cratering efficiency when impacting a weak target. In total, we show evidence for a projectile geometry effect on deflection efficiency that may inform the next generation kinetic impactor.

ACKNOWLEDGEMENTS

The authors would like to acknowledge funding from NASA YORPD (Grant Number 80NSSC22K0242).

REFERENCES

[1] A. F. Cheng, A. S. Rivkin, P. Michel, J. Atchison, O. Barnouin, L. Benner, N. L. Chabot, C. Ernst, E. G. Fahnestock, M. Kueppers, P. Pravec, E. Rainey, D. C. Richardson, A. M. Stickle, C. Thomas, *Planetary and Space Science* **2018**, *157*, 104.

[2] D. P. S. Dearborn, P. L. Miller, In *Handbook of Cosmic Hazards and Planetary Defense* (Eds.: Pelton, J. N.; Allahdadi, F.), Springer International Publishing, Cham, **2015**, pp. 733–754.

[3] National Research Council, *Defending Planet Earth: Near-Earth-Object Surveys and Hazard Mitigation Strategies*, **2010**.

[4] M. E. DeCoster, E. S. G. Rainey, T. W. Rosch, A. M. Stickle, *Planet. Sci. J.* **2022**, *3*, 186.

[5] S. D. Raducan, M. Jutzi, T. M. Davison, M. E. DeCoster, D. M. Graninger, J. M. Owen, A. M. Stickle, G. S. Collins, *International Journal of Impact Engineering* **2022**, 104147.

[6] M. Bruck Syal, J. Michael Owen, P. L. Miller, *Icarus* **2016**, *269*, 50.

[7] J. D. Walker, S. Chocron, D. D. Durda, D. J. Grosch, N. Movshovitz, D. C. Richardson, E. Asphaug, *Hypervelocity Impact Sciety* **2013**, *58*, 240.

[8] A. F. Cheng, P. Michel, M. Jutzi, A. S. Rivkin, A. Stickle, O. Barnouin, C. Ernst, J. Atchison, P. Pravec, D. C. Richardson, *Planetary and Space Science* **2016**, *121*, 27.

[9] A. M. Stickle, M. Bruck Syal, A. F. Cheng, G. S. Collins, T. M. Davison, G. Gisler, N. Güldemeister, T. Heberling, R. Luther, P. Michel, P. Miller, J. M. Owen, E. S. G. Rainey, A. S. Rivkin, T. Rosch, K. Wünnemann, *Icarus* **2020**, *338*, 113446.

[10] S. D. Raducan, T. M. Davison, R. Luther, G. S. Collins, *Icarus* **2019**, *329*, 282.

[11] A. M. Stickle, J. A. Atchison, O. S. Barnouin, A. F. Cheng, D. A. Crawford, C. M. Ernst, Z. Fletcher, A. S. Rivkin, *Procedia Engineering* **2015**, *103*, 577.

[12] T. G. Trucano, J. M. McGlaun, *International Journal of Impact Engineering* **1990**, *10*, 601.

[13] E. Pierazzo, N. Artemieva, E. Asphaug, E. C. Baldwin, J. Cazamias, R. Coker, G. S. Collins, D. A. Crawford, T. Davison, D. Elbeshausen, K. A. Holsapple, K. R. Housen, D. G. Korycansky, K. Wünnemann, *Meteoritics & Planetary Science* **2008**, *43*, 1917.

[14] D. Crawford, *Adaptive Mesh Refinement in CTH*, Sandia National Laboratories (SNL), Albuquerque, NM, and Livermore, CA, **1999**.

[15] J. M. McGlaun, S. L. Thompson, M. G. Elrick, *International Journal of Impact Engineering* **1990**, *10*, 351.

[16] E. S. G. Rainey, A. M. Stickle, A. F. Cheng, A. S. Rivkin, N. L. Chabot, O. S. Barnouin, C. M. Ernst, *International Journal of Impact Engineering* **2020**, *142*, 103528.

[17] B. Jean, T. L. Rollins, *AIAAJ* **1970**, *8*, 1742.

[18] B. Jean, *AIAA Journal* **1966**, *4*, 1854.

[19] SESAME '83: report on the Los Alamos Equation-of-State Library, Los Alamos National Lab., NM (USA), United States, **1983**.

[20] J. Barnes, *SESAME equation of state*, Los Alamos National Lab. (LANL), Los Alamos, NM (United States), **1985**.

[21] T. Heberling, G. Terrones, W. Weseloh, *International Journal of Impact Engineering* **2018**, *122*, 1.

[22] E. S. Hertel, R. L. Bell, M. G. Elrick, A. V. Farnsworth, G. I. Kerley, J. M. McGlaun, S. V. Petney, S. A. Silling, P. A. Taylor, L. Yarrington, In *Shock Waves @ Marseille I* (Eds.: Brun, R.; Dumitrescu, L. Z.), Springer, Berlin, Heidelberg, **1995**, pp. 377–382.

[23] D. J. Steinberg, C. M. Lund, *Journal of Applied Physics* **1989**, *65*, 1528.

[24] P. A. Taylor, *CTH Reference Manual: The Steinberg-Guinan-Lund Viscoplastic Model*, Sandia National Laboratories (SNL), Albuquerque, NM, **1992**, p. 47.

[25] N. Sakatani, S. Tanaka, T. Okada, T. Fukuhara, L. Riu, et al., *Nat Astron* **2021**, *5*, 766.

[26] D. J. Scheeres, J. W. McMahon, A. S. French, D. N. Brack, S. R. Chesley, D. Farnocchia, Y. Takahashi, J. M. Leonard, J. Geeraert, B. Page, P. Antreasian, K. Getzandanner, D. Rowlands, E. M. Mazarico, J. Small, D. E. Highsmith, M. Moreau, J. P. Emery, B. Rozitis, M. Hirabayashi, P. Sánchez, S. Van wal, P. Tricarico, R.-L. Ballouz, C. L. Johnson, M. M. Al Asad, H. C. M. Susorney, O. S. Barnouin, M. G. Daly, J. A. Seabrook, R. W. Gaskell, E. E. Palmer, J. R. Weirich, K. J. Walsh, E. R. Jawin, E. B. Bierhaus, P. Michel, W. F. Bottke, M. C. Nolan, H. C. Connolly, D. S. Lauretta, *Nat Astron* **2019**, *3*, 352.

[27] M. Jutzi, P. Michel, K. Hiraoka, A. M. Nakamura, W. Benz, *Icarus* **2009**, *201*, 802.

[28] J. Castillo-Rogez, E. D. Young, In *Planetesimals: Early Differentiation and Consequences for Planets* (Eds.: Weiss, B. P.; Elkins-Tanton, L. T.), Cambridge University Press, Cambridge, **2017**, pp. 92–114.

[29] G. J. Flynn, L. B. Moore, W. Klöck, *Icarus* **1999**, *142*, 97.

[30] D. T. Britt, D. Yeomans, K. Housen, G. Consolmagno, *Asteroid Density, Porosity, and Structure*, **2002**.

[31] A. Fujiwara, J. Kawaguchi, D. K. Yeomans, M. Abe, T. Mukai, T. Okada, J. Saito, H. Yano, M. Yoshikawa, D. J. Scheeres, O. Barnouin-Jha, A. F. Cheng, H. Demura, R. W. Gaskell, N. Hirata, H. Ikeda, T. Kominato, H. Miyamoto, A. M. Nakamura, N. Nakamura, K. Sasaki, K. Uesugi, *Science* **2006**, *312*, 1330.

[32] R. A. Schultz, *Journal of Structural Geology* **1996**, *18*, 1139.

[33] J. D. Walker, S. Chocron, *International Journal of Impact Engineering* **2011**, *38*, A1.

[34] D. A. Crawford, P. H. Schultz, **2013**, *1737*, 3047.

[35] P. H. Schultz, D. A. Crawford, *Nature* **2016**, *535*, 391.

[36] G. S. Collins, H. J. Melosh, B. A. Ivanov, *Meteoritics & Planetary Science* **2004**, *39*, 217.

[37] D. Elbeshausen, K. Wünnemann, G. S. Collins, *Icarus* **2009**, *204*, 716.